MODELLING FRONTAL CLOUDS WITH THE CNRM CLOUD-RESOLVING MODEL

J.L.Redelsperger

Centre National de Recherches Météorologiques
(Météo-France and CNRS)

SUMMARY

An anelastic non–hydrostatic cloud model is used to study both idealized and real cases of cold fronts. The general features of the 3D model together with the specific points of the 2D frontal version are shortly described. Results of moist numerical experiments using an analytical solution to the Eady problem as the initial condition are summarized. Two-dimensional and three-dimensional numerical experiments of frontal systems corresponding to the 2th and 7th Intensive Observing Period (IOP 2 and IOP 7) of the FRONTS 87 experiment are presented. Comparaisons to Doppler radar observations performed during FRONTS 87 are discussed together with sensitivity studies to large scale forcings and horizontal resolution, allowing the determination of the physical mechanisms producing the wide rainbands in the IOP2 case. The budgets of apparent heat, moisture and horizontal momentum sources/sinks for the IOP2 case, are finally discussed in details, with regard to their parameterization in large scale models.

1 INTRODUCTION

Over the last two decades much progress has been made in understanding the physical processes involved in frontogenesis, which is generally a consequence of the development of a baroclinic wave and involves a cascade of energy from large to small scales. The primary and secondary processes in frontogenesis take place both at synoptic and mesoscale. In the presence of moisture, the ageostrophic circulation leads to the formation of clouds and precipitation, which is related to processes occurring at both mesoscale and smaller scales. Field campaigns have shown that there is a wealth of small scale and mesoscale phenomena associated with extratropical frontal systems (e.g. Browning and Harrold 1970; Houze *et al.* 1976; Hobbs 1978; Parsons and Hobbs 1983). Cold fronts have been extensively documented since they lead to the significant features: sharp thermal contrasts, strong surface-level winds, and high precipitation rates.

The ability of operational numerical models to forecast the occurrence of the rainbands and other significant mesoscale features cited above is poor. In addition, frontal evolution in these operational models can be dramatically affected by the large errors in the description of dynamical and physical fields at mesoscale, due to spurious heat and momentum transfers. It is thus important to determine the improvements necessary in forecast models in order to correctly describe such rainbands. Various simulations have demonstrated the importance of the release of latent heat in extratropical systems (e.g. Maddox 1980; Chang *et al.* 1981; Ross and Orlanski 1978; Hsie and Anthes 1984). With increasing available computing power, it is possible to consider high resolution simulations of frontogenesis using the more general non–hydrostatic system (Gall *et al.* 1987; Bénard *et al.* 1992 a and b; Dudhia 1993). This approach has the advantage of explicitly resolving the convection and the large scale flow in the same framework. It is the main purpose of the paper to show that high horizontal and vertical resolution together with explicit representation of cloud processes allow the simulation of both narrow and wide frontal rainbands observed in the vicinity of real fronts, despite starting from large–scale flow. The second purpose is to present one example

of using such CRM (cloud-resolving model) simulations to perform budget of various parameters in order to test or develop parameterizations of cloud processes in GCMs (see Science Plan of GEWEX Cloud System Study , 1994).

In this paper, the anelastic non–hydrostatic model developed by Redelsperger and Sommeria (1986) is used to study both idealized and real cases of cold fronts. The general features of the 3D model together with the specific points of the 2D frontal version are given in section 2. Main results of moist numerical experiments using an analytical solution to the Eady problem as the initial condition are summarized in section 3. Two-dimensional and three-dimensional numerical experiments of frontal systems corresponding to the 2th and 7th Intensive Observing Period (IOP 2 and IOP 7) of the FRONTS 87 experiment are presented in sections 4 and 5, respectively. That also includes comparaisons to Doppler radar observations performed during FRONTS 87 and sensitivity studies to large scale forcings and horizontal resolution, allowing the determination of the physical mechanisms producing the wide rainbands. The budgets of apparent heat, moisture and horizontal momentum sources/sinks for the IOP2 case, are finally discussed in section 6, with regard to their parameterization in large scale models.

2 THE CLOUD-RESOLVING MODEL

2a General features

The three–dimensional cloud model is described in detail by Redelsperger and Sommeria (1981, 1986). The governing system is the primitive non-hydrostatic anelastic set of equations. The spatial discretization is of second order on an Arakawa type–C grid and it uses the leap–frog temporal scheme. A temporal filter (Asselin, 1972) and a fourth order horizontal diffusion operator (as described in Redelsperger and Lafore, 1988) are applied to the prognostic variables in order to damp short temporal and spatial oscillations, respectively.

The parameterization scheme for subgrid–scale turbulence is based on an assumption of zero third–order moments in the basic equations. The second–order moments are expressed as a function of the turbulent kinetic energy, which is given by a prognostic equation (see Redelsperger and Sommeria, 1981 for details). One advantage of this scheme is a correct description of anisotropic turbulent exchanges in stable layers, which is not the case with simpler formulations. A modification has been made to the scheme to distinguish the horizontal and vertical mixing length in the second–order momentum equations, as the horizontal mesh size is much larger than the vertical.

The subgrid fluctuations of the thermodynamic variables are taken into account in the condensation and evaporation (C.E) scheme, to allow for partial condensation over grid volumes. This is an important feature, since the hypothesis of complete C.E in grid volumes is unrealistic with grid meshes larger than 1 km (Sommeria and Deardorff, 1977). In addition, the C.E scheme and the subgrid turbulent parameterization are formulated in terms of temperature and water variables which are conserved to a good approximation through C.E processes. Such an approach allows an implicit correlation between basic variables and microphysical production terms (see Redelsperger and Sommeria, 1982 for details).

A Kessler–type parameterization is used for the microphysical production and exchange terms. The basic assumptions concerning the precipitation scheme are:

- The ice phase is not considered in present studies; a parameterization is currently available in the model (Caniaux *et al.* 1994a), but not included in the present simulations for sake of simplicity.
- The drops are subdivided into two classes: cloud droplets and rain drops (whose specific contents are q_c and q_r respectively);

- A threshold value (0.5 x 10^{-3} kg kg^{-1}) for the autoconversion from cloud water into rain water is assumed and is modulated by the subgrid variance of q_c.
- A Marshall-Palmer distribution is assumed for raindrops; this distribution is used to determine a mean terminal velocity for the raindrop population.

In all experiments, the vertical coordinate is stretched with a mesh interval measuring from 60 m near the ground to 500 m above the cloud layer. In the FRONTS 87 simulations, the model uses open lateral boundary conditions but uses a method suggested by Carpenter (1982) to monitor the large scale forcing (Redelsperger and Lafore 1988; Cailly *et al.* 1994), computed from larger scale "Péridot" or ARPEGE model. For the Eady problem, the domain is periodic in the cross-frontal direction.

2b The 2D frontal version

In the simulations of Eady problem and FRONTS87-IOP2 cases, a particular two–dimensional version of the model is used in order to look in details at the relationship between rainband occurrences, and large–scale forcing (namely the along–front deformation and baroclinicity). The model equations have to be modified to take into account the large–scale gradients along the front (y–direction) in the two–dimensional framework. The anelastic continuity equation is written as:

$$\frac{\partial u}{\partial x} + \left(\frac{\partial v}{\partial y}\right)_{LS} + \frac{1}{<\rho>}\frac{\partial <\rho> w}{\partial z} = 0 \qquad (1)$$

where $\left(\frac{\partial v}{\partial y}\right)_{LS}$ is the along–front large–scale divergence, $<\rho>$ is the density and the brackets denote horizontal averaging over the domain. The momentum equations, written in flux form, have to be modified to take into account this new continuity equation. The equation for the along–front momentum also includes the large–scale pressure gradient in the y-direction, through the geostrophic wind U_g.

$$\frac{\partial u}{\partial t} = -\frac{\partial u^2}{\partial x} - \frac{1}{<\rho>}\frac{\partial (<\rho>\, uw)}{\partial z} - u\left(\frac{\partial v}{\partial y}\right)_{LS} \quad -C_p <\rho><\theta_v>\frac{\partial \pi'}{\partial x} + f\, v \quad +D_u \qquad (2)$$

$$\frac{\partial v}{\partial t} = -\frac{\partial uv}{\partial x} - \frac{1}{<\rho>}\frac{\partial (<\rho>\, vw)}{\partial z} - 2v\left(\frac{\partial v}{\partial y}\right)_{LS} \quad -f\,(u - U_g) \quad +D_v \qquad (3)$$

$$\frac{\partial w}{\partial t} = -\frac{\partial uw}{\partial x} - \frac{1}{<\rho>}\frac{\partial (<\rho>\, w^2)}{\partial z} - w\left(\frac{\partial v}{\partial y}\right)_{LS} \quad -C_p <\rho><\theta_v>\frac{\partial \pi'}{\partial z} + g\frac{\theta_v'}{<\theta_v>} \quad +D_w \qquad (4)$$

In these equations, π is the Exner pressure, f the Coriolis parameter, θ_v the virtual potential temperature, ($\theta_v = \theta + \alpha\theta q$), C_p the specific heat at constant pressure, α a constant ($\alpha = .608$) and D_X the subgrid–scale transport of variable X. The prime quantities correspond to deviations from the horizontal average on the simulation domain. Owing to the present two–dimensional framework, the large–scale term $\left(\frac{\partial u}{\partial y}\right)_{LS}$ is neglected. Examination of this term in the IOP2 case indicates weak values up to mid–troposphere. However at upper levels, significant values are found in the upper level jet. The equation for potential temperature includes modifications both due to the new continuity equation and due to the along–front large scale baroclinicity, $\left(\frac{\partial \theta}{\partial y}\right)_{LS}$:

$$\frac{\partial \theta}{\partial t} = -\frac{\partial \theta u}{\partial x} - \frac{1}{<\rho>}\frac{\partial (<\rho>\theta w)}{\partial z} - \theta\left(\frac{\partial v}{\partial y}\right)_{LS} - v\left(\frac{\partial \theta}{\partial y}\right)_{LS} + D_\theta + Q_\theta \qquad (5)$$

where Q_θ is the diabatic source/sink term. Equations for water conservation have also been modified in the same way, but are not reproduced here. The thermal wind balance in the y-direction, written

in the anelastic system, is used in order to relate the along–front baroclinicity and the geostrophic wind:

$$\frac{g}{<\theta_v>}\left(\frac{\partial \theta_v}{\partial y}\right)_{LS} = f\left(\frac{\partial}{\partial z} - \frac{1}{<\theta_v>}\frac{\partial \theta_v}{\partial z}\right) U_g \tag{6}$$

The along–front baroclinicity may be expressed as a function of the along–front gradients of the potential temperature θ and the specific humidity q:

$$\left(\frac{\partial \theta_v}{\partial y}\right)_{LS} = (1 + \epsilon\, q)\left(\frac{\partial \theta}{\partial y}\right)_{LS} + \epsilon\, \theta \left(\frac{\partial q}{\partial y}\right)_{LS} \tag{7}$$

Finally, the following continuity equation is used to determine the along–front large scale divergence $\left(\frac{\partial v}{\partial y}\right)_{LS}$ from the geostrophic wind:

$$\frac{\partial U_g}{\partial x} + \left(\frac{\partial v}{\partial y}\right)_{LS} = 0 \tag{8}$$

3 EADY PROBLEM

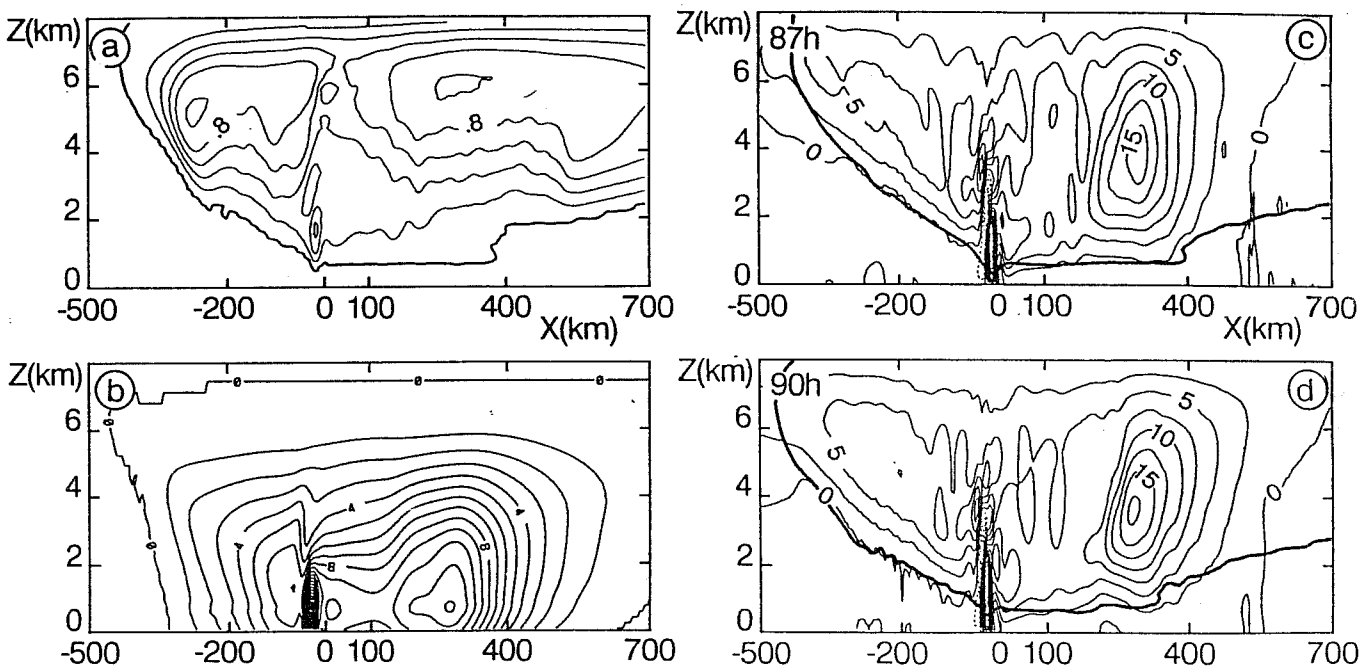

Figure 1: Cross sections of respectively, for the EADY experiment for (a) cloud water content q_c at 87 h (contour interval 0.2 x 10^{-3} g g^{-1}), (b) rainwater content q_r at 87 h (contour interval 1. x 10^{-5} g g^{-1}), (c) and (d)vertical velocity w at 87 h and 90 h, respectively (contour interval 2.5 cm s^{-1}). The heavy line on Figs (c) and (d) represents the cloud outline. (from Bénard *et al.* 1992a)

Before to simulate FRONTS 87 cases, a series of idealized numerical experiments with 5km horizontal resolution have been performed using an analytical solution to the Eady problem as the initial condition (Bénard *et al.* 1992a, 1992b; Lafore *et al.* 1994). The two–dimensional version of model just described above is used to simulate moist frontogenesis in an idealized baroclinic wave (Eady problem). An accurate representation of physical processes was found necessary to achieve a good description of frontal rainbands. Furthermore, high horizontal and vertical resolution allow the simulation of both narrow and wide frontal rainbands as observed in the vicinity of real fronts (Fig. 1).

As schematically summarized in Fig. 2, four types of bands have been clearly identified.

– A *Narrow Cold-frontal Rainband* located at the surface cold front (Fig. 2). As in real frontal systems, it mainly consists of a line of shallow convection triggered by the frictionally induced instability in the boundary layer at the surface front. The associated precipitation is heavy and organized in a narrow line. Latent heating due to condensation contributes in large part to the tilting of isentropes and to the increasing of the vertical jet strength. Sensitivity experiments show that both surface friction and condensation processes are important for the occurrence of this jet. Indeed, as found by Keyser and Anthes (1982) as well, when condensation processes are not considered, the development of the jet is sensitive to the time friction is turned on. A simulation with a 5 km horizontal resolution reproduced a vertical jet with intensity and width in good agreement with observations. Simulations with 1 km horizontal resolution are probably necessary to attain a better agreement.

– *Narrow Free-Atmosphere Rainbands* were observed over the narrow cold–frontal band (Figs. 1 and 2). A regular series of updrafts and downdrafts were generated in the stable free atmosphere above the convection line, along the frontal surface. The examination of the stability and equivalent potential vorticity structure allowed us to exclude the conditional convective instability as well the conditional symmetric instability as agents in their development. Detailed analysis suggest that the linear stationary hydrostatic gravity wave theory may explain most of the features of these bands. As predicted by the linear theory and as shown in this paper by simulations with different basic states, the vertical wavelength is highly variable. The horizontal wavelength is shown to be related to the width of the vertical jet and independent of model horizontal resolution. In addition, the position of a potential steering level and critical layer (if such exists) has to be considered in real systems to consider a possible gravity wave activity and associated mechanisms such as trapping, ducting and scale selection of these waves.

– *Wide Cold–frontal Rainbands* consist of bands periodically repeated in the frontal zone (Figs. 1 and 2). Their typical width was 75–100 km with maximum vertical velocity about 0.1 m s^{-1}. Their lifetime was limited to 6–9 hours. Subsequently a large area of slantwise convection occurs in the frontal region up to the end of the simulation.

– A *Warm–sector Wide Rainband* is a single band, located in the warm sector, at 300–400 km ahead of the surface cold front. Its width varies through simulation time from 80 km up to 250 km with a maximum vertical velocity of 0.2 m s^{-1}. This band led to widespread precipitation on a 80–120 km width. This band was present in all wet simulations from the end of upright convective adjustment up to the end of the simulation.

A budget of the Moist Potential Vorticity (MPV) has been implemented for a rigourous investigation of generating mechanisms of wide rainbands. The balance between sources, transport and evolution of MPV in the model has been first successfully validated. The parameterized turbulent subgrid–scale processes represent the main MPV source in these simulations, especially at the PBL top. It was shown that friction acts as a source of intense MPV vertical flux at the ground, maximum below the along–front low level jets in both warm and cold air masses. An intense positive MPV anomaly is obtained in the warm sector, appears to be generated by frictional processes in the far pre-frontal zone, and is then transported towards the frontal system. This anomaly induces an intensification of the along–front low level jet on its warm flank. In the present shear–driven case, this jet corresponds to a maximum of warm moist advection: the warm conveyor belt, resulting in the formation of the warm sector wide rainband located 300 km ahead the surface cold front, lies in a region of strong to weak moist symmetric stability.

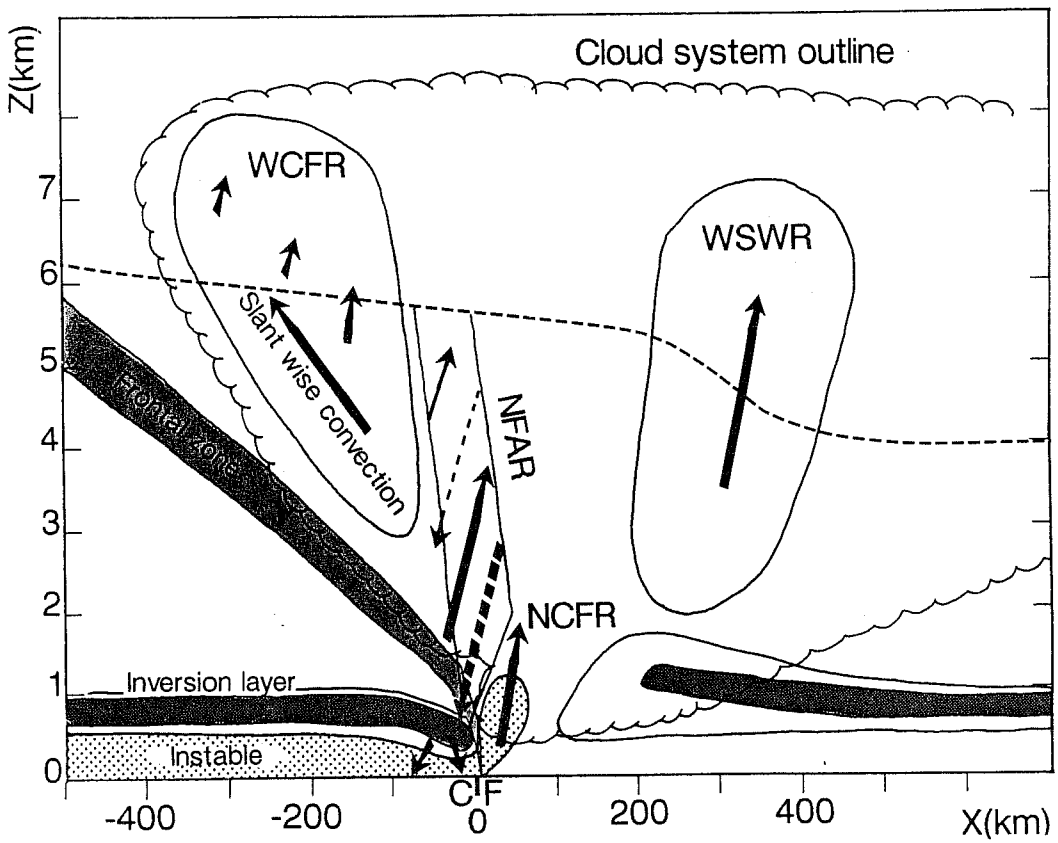

Figure 2: Schematic representation of the different bands occurring in the EADY experiments. The black region represents the inversion layer as region of convective instability is shaded. (from Bénard *et al.* 1992a)

Wide cold frontal rainbands on the other hand occur in a region of moist symmetric instability, which thus seems to enhance the circulation forced by the geostrophic shearing deformation and frictional convergence, in the frontal zone and favours the development of these bands. They efficiently transport the lowest MPV values upward, and are thus diffusive. We suggest that these bands were initiated by the dissipation of convective cells generated during the previous convective stage.

These papers are the first important step in the high–resolution simulations of observed fronts. From these results, we see that though accurate parameterizations and high resolution are both necessary to simulate the narrow bands, high resolution is less important to obtain the wide rainbands. They have indeed been obtained in our simulations with a horizontal resolution of 40 km (comparable to some regional forecast model ones), although not as distinct.

4 IOP2 of FRONTS87 experiment

The cloud-resolving model, having been validated on the idealized case of the EADY problem, is used to simulate cold front cases observed during the FRONTS87 exeperiment. First the IOP2 case is simulated in a two-dimensional framework (this section), together with extensive sensitive tests in order to determine the relationship between the large–scale along-front gradients and the rainbands (thanks to the 2D framework). Second the IOP7 case is simulated with a three-dimensional domain, taking special care with initialization and large scale coupling (section 5).

4a Initial conditions

The model domain is 3000 km × 15 km, with a horizontal resolution of 5 km. The model uses open lateral boundary conditions in x (cross-front) but including large scale forcings, computed from larger scale "Péridot" model. A Galilean transformation is applied to the horizontal velocity field with a speed of 15 m s^{-1} along the x and y directions.

The IOP2 case was first simulated using the mesoscale forecast "Péridot" model with a horizontal resolution of 35 km (Lalaurette 1991). The 6h forecast fields from "Péridot" using an European domain at 18 UTC on the 11 November 1987, are used both to initialize the non–hydrostatic model and to specify the large scale forcings through a one–way coupling between the two models. These "Péridot" fields were first interpolated onto a cartesian domain, perpendicular to the surface front, and then averaged on y-slice (along-front) of 300 km where the observed front was nearly two–dimensional, to give initial fields of the non-hydrostatic cloud model.

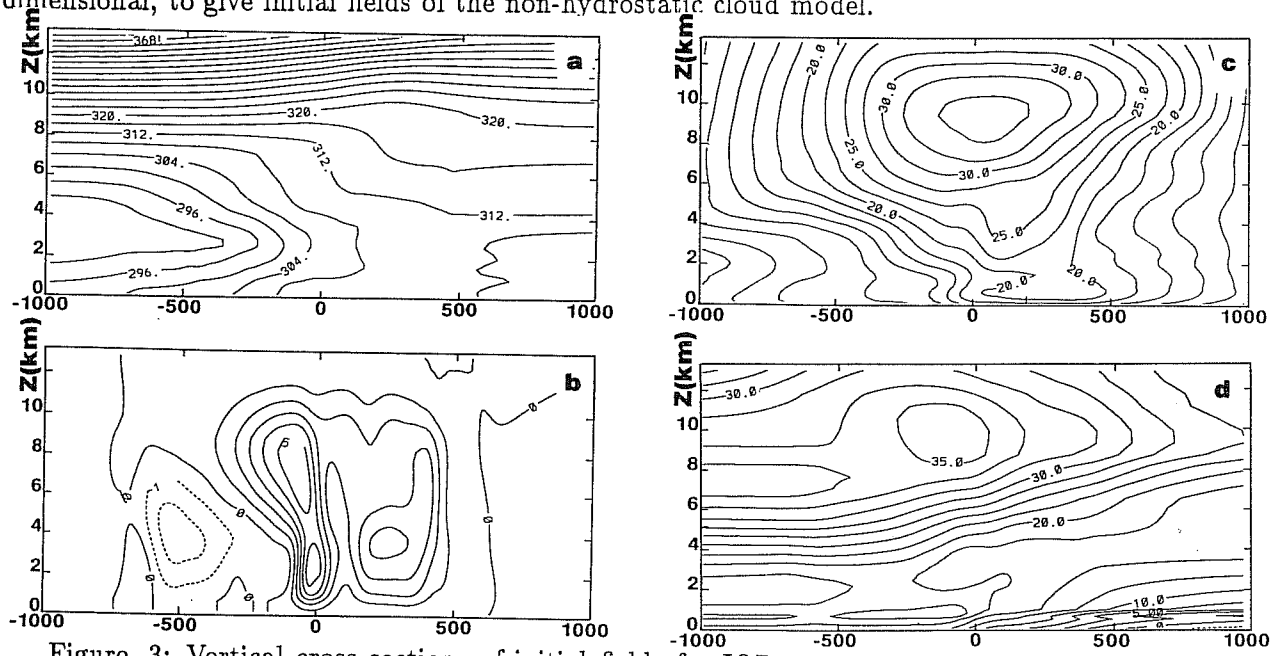

Figure 3: Vertical cross sections of initial fields for IOP2 case: (a)equivalent potential temperature (interval 4°K); (b) vertical velocity (interval 1 cm s^{-1}); (c) along–front wind and (d) cross–front wind (interval 2.5 m s^{-1}). The SCF is positioned around X=0. (from Redelsperger and Lafore 1994)

Fig. 3 shows the two–dimensional initial fields. The cold and warm sectors are easily identified on the cross–section of the equivalent potential temperature θ_e (Fig. 3a), with a well–defined region of horizontal cross–front gradient up to 3°K/100km, separating the two air masses. This region slopes with height and has a nose–shaped aspect at 2.7 km altitude. A upright, potentially unstable zone ($\partial\theta_e/\partial z < 0$) is present in the cold sector at low levels up to 2.5 km, and in the warm sector up to 2.1 km. The surface cold front (hereafter called SCF) is weak. The cold and warm sectors respectively correspond to dry and moist regions. The main region of baroclinicity across the front is located at heights between 2 and 6 km. Two maxima or jets are seen in the along–front wind component (Fig. 3c). There are the low–level jet ahead of the SCF at 1 km altitude (maximum 21 m s^{-1}) and the upper–level jet at 9.5 km (maximum 35 m s^{-1}). The cross-front wind component (Fig. 3d) shows a shallow layer (2 km) of warm and moist air flowing toward the SCF. However, the depth of this layer decreases closer to the SCF. The horizontal extent of this layer is underestimated, as compared to observations(Chong *et al.* 1991). The corresponding vertical velocity field deduced from the "Péridot" forecast (Fig. 3c) is characterized by a main ascent in phase with the SCF with a maximum of 5 cm s^{-1}. An ascent is also present in the warm sector, but wider (350 km) and slightly less intense.

The large scale along–front divergence and baroclinicity (not shown) exhibit maxima at middle and upper levels. The baroclinicity induces the most important along–front forcing, with values up to -1.75°K/100km near 5.5 km altitude, as the along–front divergence maximum (3 m s^{-1}/100km) is located at 10 km altitude in the warm sector. Below 2.5 km, the along–front gradients are weak, except in a small convergence zone 400 km ahead of the SCF.

4b Reference simulation

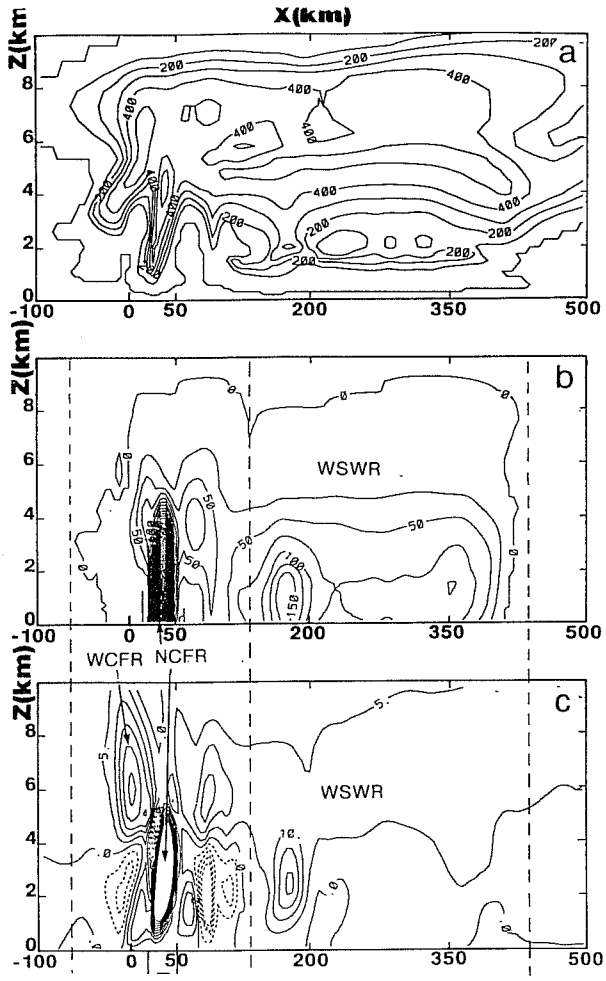

Figure 4: Cross sections showing the central part of the simulation domain for IOP2 case, at t = 4h: (a) specific cloud water content (interval 0.1 g kg^{-1}); (b) specific rain water content (interval 0.025 g kg^{-1}); (c) vertical velocity (interval 5 cm s^{-1}; values greater than .5 m s^{-1} are not plotted) (from Redelsperger and Lafore 1994)

Starting from the fields described above, a series of numerical experiments have been performed with oceanic surface conditions (more details in Redelsperger and Lafore 1994). The control experiment needs about 3 hours to reach a nearly steady state in response to the large–scale stationary forcings. The model reproduces a variety of frontal bands (Fig. 4), starting simply from the meso-α scale fields. The Narrow Cold–Frontal Rainband (NCFR) with a maximum vertical velocity of 1.45 m s^{-1} is identified at the SCF. Two classes of wide bands are also observed : a wide cold–frontal rainband and warm sector wide rainbands producing less precipitation and weaker vertical velocities of around .2 m s^{-1}.

The NCFR consists of shallow convection associated with heavy and localized rainfall (Fig. 4b). The band moves eastward at the same speed as the SCF, and its vertical extent is limited to the lowermost 4 km, due to prevailing upright potentially unstable conditions. It is noted that the model is able to generate intense temperature gradients (1°K/10km) and cross–front vorticity (about 10f) in phase with the SCF and the NCFR. These observed characteristic features were indeed not present in the initial fields.

The simulated wide bands produce less dramatic changes but occur on a larger scale. The Wide Cold–Frontal Rainband (WCFR) consists of an ascent positioned along the cold front with a intensity maximum of .25 m s^{-1} (Fig. 4c). Condensation and precipitation (Fig. 4a and b) are associated with this ascent, but are insufficient to produce significant precipitation at the ground. Most precipitation evaporates between 2 and 4 km, activating a well–defined downdraft just under the updraft corresponding to the WCFR (Fig. 4c). The ascent is positioned in the cold frontal region where temperature gradient and along–front gradient are strong, and where upright potential stability prevails. Looking at the effective symmetric stability condition indicates that only a small part of the band is in a region of CSI.

In the warm sector, several Warm Sector Wide Rainbands (WSWR) may be identified in the vertical velocity and rain fields (Figs. 4b and c). The first corresponds to an ascent positioned 150 km ahead of the SCF. This updraft region is limited to the first 4 km of the atmosphere with an maximum intensity of .2 m s^{-1} and corresponds to a well–marked but not very intense (maximum of .15 g kg^{-1}) rainband. This band occurs in the region of a potential convective instability maximum, which can be viewed as a second though less intense surface discontinuity, as observed from the surface network and dropsondes (Thorpe and Clough, 1991). The second type of ascent is more classical in producing rather stratiform precipitation. Upward motion is generated in this region on a 400 km horizontal extent and between 4 and 8 km altitude. Individual cores may be distinguished within this extensive region, giving two rain maxima. As for the WCFR analyzed above, except for a thin layer in its upper part, these bands occur in a gravitationally and symmetrically stable region. Again, these bands are driven by the along–front large–scale gradients.

4c Comparisons with observations

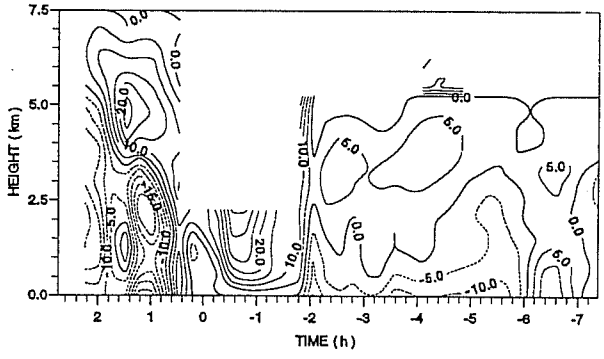

Figure 5: Vertical cross sections deduced by the VAD analysis of vertical velocity for IOP2 case (interval 5 cm s^{-1}). (from Redelsperger and Lafore 1994)

Doppler radar observations were performed between 1200 and 2400 UTC during IOP 2 of the FRONTS 87 experiment (Chong *et al.* 1991). In the warm sector, 200 km ahead the SCF, mesoscale banded structure was observed with embedded rainbands 50 km wide and with reflectivities in excess of 30 dBZ. A 5 km narrow band at the SCF (NCFR) was identified, preceding a 50 km wide rainband (WCFR). Vertical Azimuthal Display (VAD) analysis of successive Doppler radar observations allow the determination of this kinematic structure at the mesoscale. Fig. 5 shows a composite of these observations made at successive times with a diameter of the VAD circle around 40 km. Therein, the time–height sections have been considered as a distance–height section, normal to the front, assuming a constant front speed of 11 m s^{-1}. In explicitly simulating both convection and large-scale flow, the model reproduces the main features of observed circulation and the large variety of bands, though several discrepancies are present. The position of the WCFR is found to be closer to the NCFR in the simulation than in the radar observations. The underestimation of descents in the simulation may be due to the omission of the ice phase in the model. The NCFR intensity is larger in the simulation than the VAD observations and is easily explained by the different horizontal resolution (5 km *vs* 40 km). In fact, the simulated maximum (1.4 m s^{-1}) for the NCFR is closer to observations made at small scale (about 3 m s^{-1}) obtained by dual–Doppler techniques with a

horizontal resolution of .5 km.

The simulated and observed precipitation patterns at the ground have been also compared. The narrow maximum of observed precipitation associated with the NCFR (12 to 20 mm h^{-1}) is well simulated (17 mm h^{-1}) by the control experiment. The model also predicts the intensity, position and width of precipitation, produced by the WSWR. In contrast, the present simulation fails to reproduce the precipitation associated with the WCFR, although the vertical velocity field shows clear evidence of a band.

4d Physical sensitivity studies

Several sensitivity experiments have been performed. Initiating the simulation with no ageostrophic flow, the cloud–resolving model is able to rebuild the ageostrophic part, although about a 1 hour lag is necessary to get the same state obtained in the control experiment. Although not general and certainly not relevant for tropical cases, the strong similarities between these experiments leads to the following conclusions (Redelsperger and Lafore 1994):

- The knowledge of the ageostrophic part is not necessary to start a simulation. It is thus possible to initialize the model from the analyzed or forecasted fields of a mesoscale model, with the divergent part from the flow removed.
- It is possible to modify the along–front large scale gradients to study their influence on the rainband occurrence, starting simulations without the ageostrophic part.

The latter point together with the two–dimensional framework, enables us to study the relationships between rainbands and along–front large scale forcings (namely the along–front deformation and baroclinicity). The main conclusions of these sensitivities studies are that for the IOP2 case:

- The along–front deformation is not important
- The along–front baroclinicity is fundamental for the structure and intensity of wide bands (WCFR and WSWR).
- The NCFR structure and intensity are weakly dependent on these forcings, both for the ground precipitation and for the amplitude of the vertical velocity.

Sensitivity studies to the horizontal resolution has been also performed (Redelsperger and Lafore 1994). Fine horizontal resolution was found necessary to describe the NCFR and its associated sharp peak of precipitation. Nevertheless, crude resolution (20 km) appears sufficient to simulate the WSWR, the total precipitation and the profiles of the apparent heat and moisture sources at the system scale. The importance of large scale forcings on convection, which is independent on the horizontal resolution, may explain this rather surprising result.

The control simulation will be used in section 6 to compute heat, moisture and momentum budgets.

5 IOP7 of FRONTS87 experiment

As shown in the previous experiments, the two-dimensionnal framework is very convenient for studying the relationship between rainbands and along-front large-scale gradients. To increase the realism of the simulations, three-dimensional simulations of frontal region are obviously necessary. This section presents another step towards this goal. It is important to point out that 3D initialization of cloud models as well their coupling with large scale model, is still in the infancy. Fo this reason, the initialization and the coupling of the present cloud model with a large scale hydrostatic model,

is presented in the following subsection (more details can be found in Cailly *et al.* 1994). In order to initialize the nested grid model, the non hydrostatic cloud model uses fields forecasted by the ARPEGE french forecast model. The present approach of nesting is to formulate open radiative boundary conditions for the normal velocity, and advective extrapolations for scalar variables.

5a Initialization and Coupling

The 3D model (hereafter NH) is used on a domain of 1200 $km \times 1800$ $km \times 14$ km, with an isotropic horizontal mesh of 30 km. The vertical coordinate z is stretched with a mesh interval measuring from 60 m near the ground to 500 m at the top, and the time step is 20s . The coarse mesh grid model (noted LSM) is the ARPEGE french operational forecast model. It is a stretched spectral model (T95 L21 C3.5), hydrostatic, based on the hybrid vertical coordinate η. The horizontal resolution in the FRONTS87 region is around .50 km. Reanalysis of IOP7 and IOP8 with the ARPEGE/CANARI system has been performed by Desroziers (1993) in including supplementary radiosoundings and dropsoundings realized during FRONTS87. The method of initialization is based on interpolations of the LSM data to the NH data without smoothing. In the first step, the part of the sphere over which the NH is to be integrated is firstly projected on a plane. In a second step, data are horizontally interpolated from the LSM grid to the NH grid. In a third step, data are vertically interpolated from the vertical hybrid grid of LSM to the vertical height of NH. As the NH model actually neglects the orography, a vertical displacement of the PBL is implemented. Fields are adjusted vertically to the NH levels by polynomial interpolation, ensuring the conservation of mass fields and mass fluxes. The vertical velocity is deduced from the integration of the anelastic continuity equation. The horizontal wind is corrected across the depth of the atmosphere to verify the zero vertical velocity condition assumed by the NH model at the upper boundary. The output of the initialization routine includes wind (U, V, W), potential temperature and specific humidity, on the z levels of the NH model.

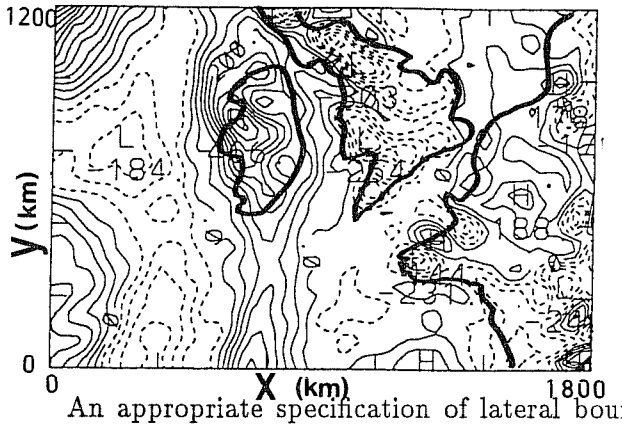

Figure 6: Horizontal cross section at 1.1 km altitude of initial vertical velocity at 6h00 UTC 9 January 1987 (IOP7 Case) (contour interval .5 cm s^{-1}) (from Cailly *et al.* 1994).

An appropriate specification of lateral boundary conditions is one of the crucial factors for a successful time integration of limited area prediction models. Extensive tests led us to choose the following method (Cailly *et al.* , 1994):

- *For scalar variables and velocity component, non normal to the boundary:* an advective extrapolation is used in distinguising inflow and outflow. At inflow, the NH fields are specified from the LSM fields by a linear interpolation in time and space, between value at the second inner point and the large scale value at a given distance of the boundary. At outflow, the fields are extrapolated from the NH inner fields.

- *Normal velocity to the boundary:* at inflow, tendencies are specified from the LSM values; at outflow, the radiation condition is used but with a generalized Sommerfeld equation allowing to take in account the LSM tendency and normal gradients of the normal velocity to the

considered boundary (Carpenter 1982; Redelsperger and Lafore 1988):

$$\frac{\partial u^{\perp}}{\partial t} = \frac{\partial u^{\perp}{}_{LSM}}{\partial t} - C^{*}(\frac{\partial u^{\perp}}{\partial n} - \frac{\partial u^{\perp}{}_{LSM}}{\partial n})$$

with $u^{\perp}$ the normal velocity, $C^{*} = C + U$, where U is the advection velocity, C a fixed phase speed. All the boundary conditions are applied once per fine-grid time step. A NH simulation is performed during $12h$, starting at 06 UTC 9 January 1988. The LSM data are updated at $3h$ intervals.

5b Preliminary results

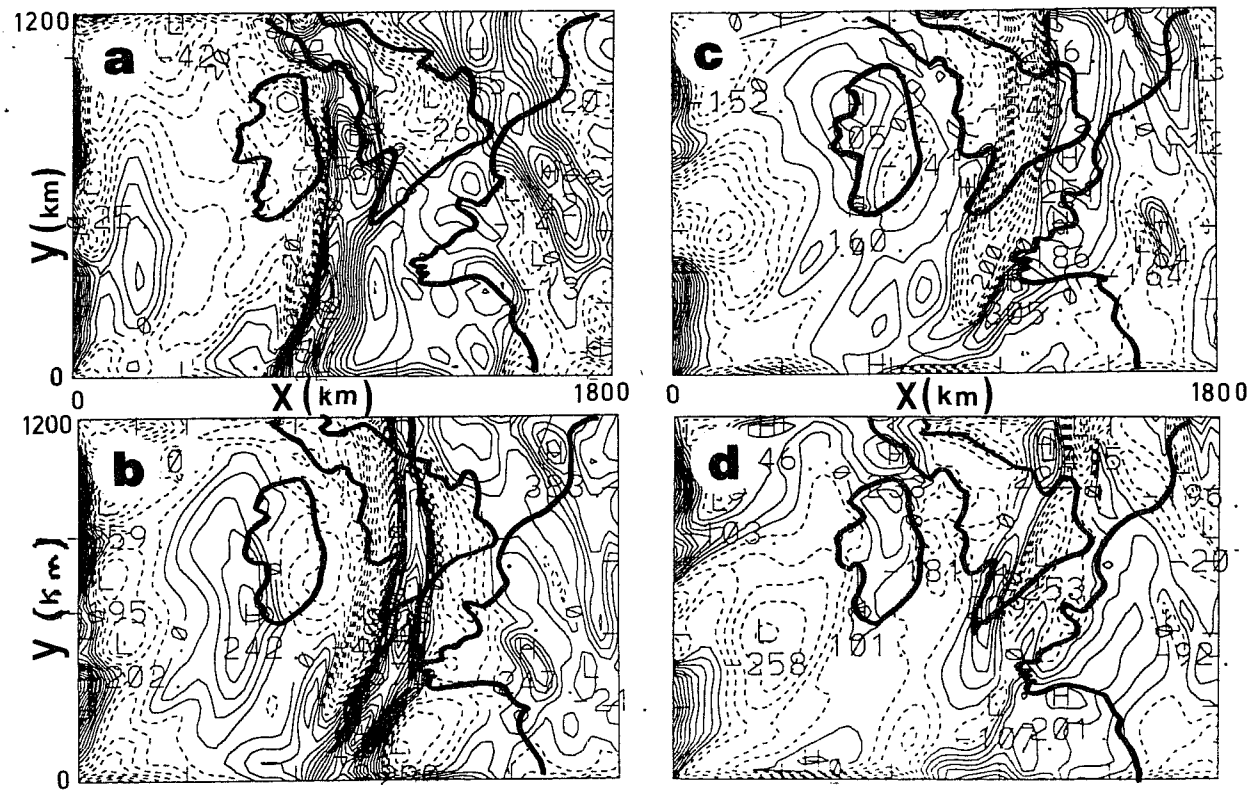

Figure 7: Horizontal cross sections of vertical velocity predicted by NH for the IOP7 case at $1,1$ km altitude: (a) $9h00$, (b) $12h00$, (c) $15h00$ and (d) $18h00$ (contour interval .5 cm s^{-1}) (from Cailly *et al.* 1994)

Figure 6 show the initial vertical velocity at 1 km height, on the NH grid interpolated from the ARPEGE forecasted fields following the procedure outlined above. The surface cold front is well marked with a position in fair agreement with observations.

Starting from the LS fields, NH is able to reproduce three rainbands corresponding to the Narrow Cold Frontal Rainband (NCFR) above the surface cold front, the Wide Cold Frontal Rainband (WCFR) and the Warm Wide Frontal Rainband (WCFR) ahead the cold front. The evolution of the NCFR position and structure can be viewed on the low level horizontal cross-sections of vertical velocity on Fig 7. The speed propagation and position is in good agreement with observations reported by Thorpe and Clough (1991), though the NH seems slightly overestimated the speed

propagation. The absence of orography representation in NH can be explained this difference.

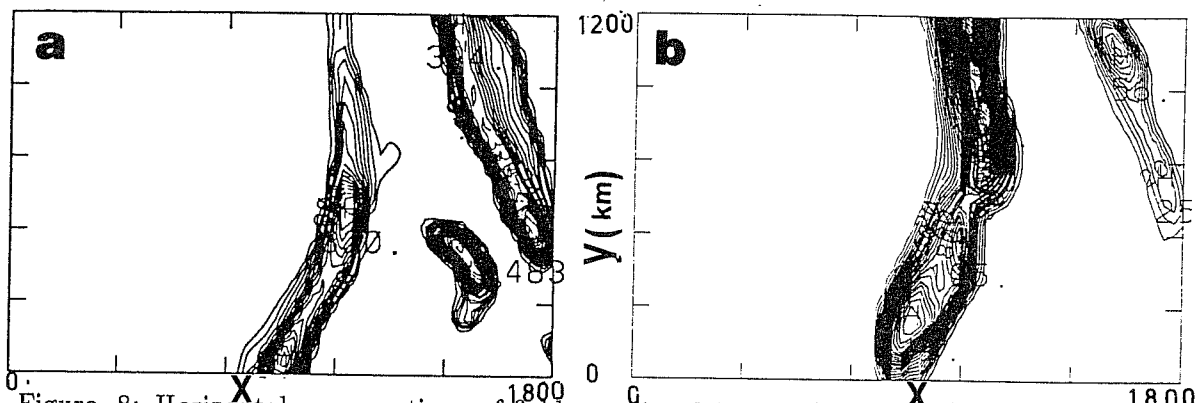

Figure 8: Horizontal cross sections of fields predicted by NH (IOP7 case) at 1,1 km altitude and at t= UTC 12h00 for: (a) cloud water content (contour interval of .02 g /kg) and (b) rainwater content (contour interval of .005 g /kg). (from Cailly *et al.* 1994)

The associated cloud and rain fields (Fig 8) show signature of type of bands, though precipitation coming from the NCFR and the WCFR merge in an unique band at ground, due to a too coarse horizontal resolution. Vertically the model reproduces some features of rainbands and observed circulation (Fig 9). The NCFR is identified with a maximum of vertical velocity, though weaker than observed. The WCFR (Wide Cold Frontal Rainband) consists of an ascent positioned along the cold front, with weaker velocity. Most associated precipitation evaporates under the updraught corresponding to the WCFR, activating a low-level downdraft. In the warm sector, an large ascent (around 300 km wide) is simulated. The WSWR is positionned 450 km ahead the surface cold front, in producing stratiform cloud with small precipitation amount at this time. Associated upward motion is generated in this region on a 350 km horizontal extent and between 3 and 10 km altitude. The along–front wind (Fig 9a) shows the low-level jet around 1 km, and the upper level jet.

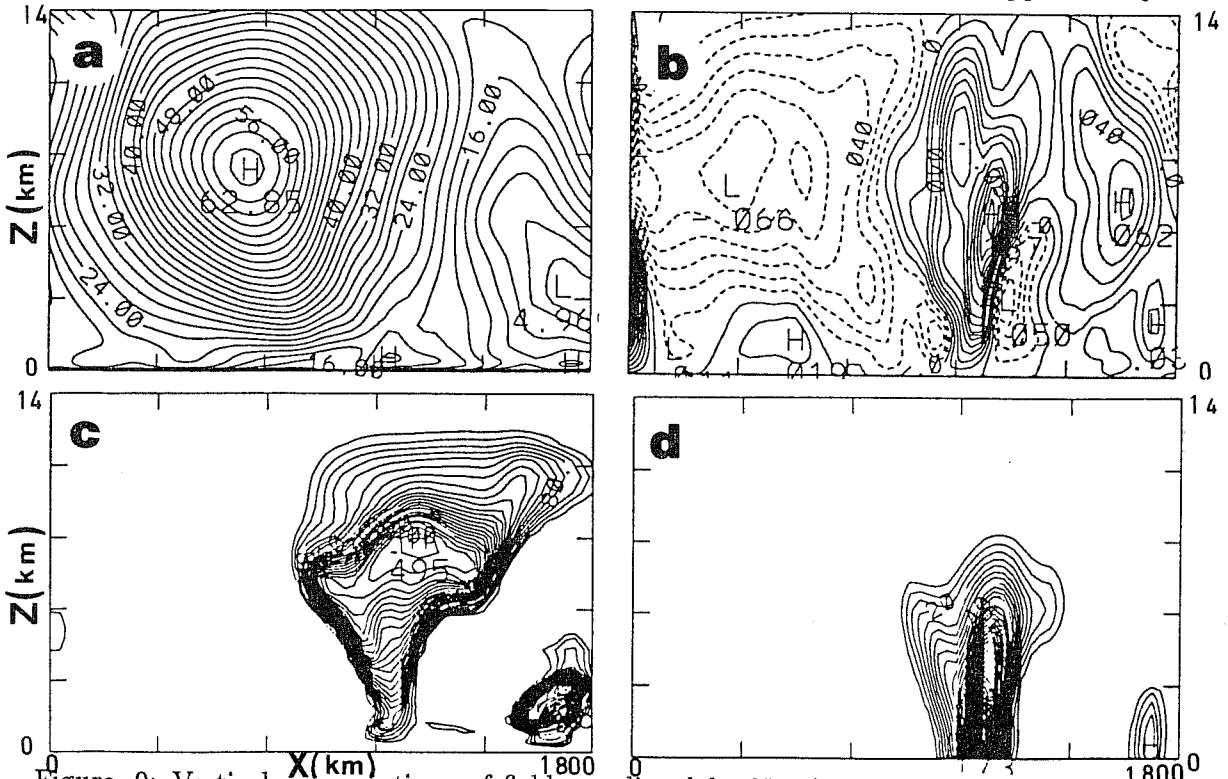

Figure 9: Vertical cross sections of fields predicted by NH (IOP7 case) at Y= 780 km and at t= UTC 12h00 for: (a) x-component wind (contour interval 2 m s^{-1}), (b) vertical velocity (contour interval 1 cm s^{-1}), (c) cloud water content (contour interval of .02 g /kg) and (d) rainwater content (contour interval of .005 g /kg). (from Cailly *et al.* 1994)

These preliminary results indicates that starting from the knowledge of large scale flow, NH is able to reproduce some features of the observed banded structure, as previously shown in a two-dimensional framework for the IOP2 case. The horizontal resolution is however not sufficient to predict correct intensity and horizontal extent of the NCFR.

6 HEAT, MOISTURE & MOMENTUM BUDGETS

One of the problems for large–scale numerical models is the parameterization of subgrid–scale precipitating cloud processes, which have a large impact on the large–scale fields of heat, moisture and momentum (e.g. Frank 1983; Johnson 1984; Browning 1990). These parameterizations are generally conceptualized and fitted from observations. The use of cloud–resolving models is another way to investigate the vertical distribution of precipitating cloud effects. Moreover, these models are able to diagnose and to explain the convective eddy transport. In the past, such works have been performed for squall lines (Lafore *et al.* 1988; Tao and Simpson 1989; Tao *et al.* 1993; Caniaux *et al.* 1994a and b), showing the full potential of this approach. Such work on frontal systems have not yet been done, for the simple reason that cloud–scale simulations were not available. In this section, the heat, moisture and momentum sources/sinks due to frontal rainbands will be presented and discussed, for the simulation of IOP2 case (section 4).

Four zones have been chosen to perform the budget calculations on the control experiment with 5km horizontal resolution (see Fig. 4c for their position). The zone labeled ZT covers the most intense part of the frontal system (500 km wide). This region ZT is subdivided in 2 regions ZA (200 km wide) and ZB (300 km wide), surrounding the cold front and in the warm sector, respectively. The γ–scale region Z (30 km wide) documents the NCFR activity.

6a Latent heating

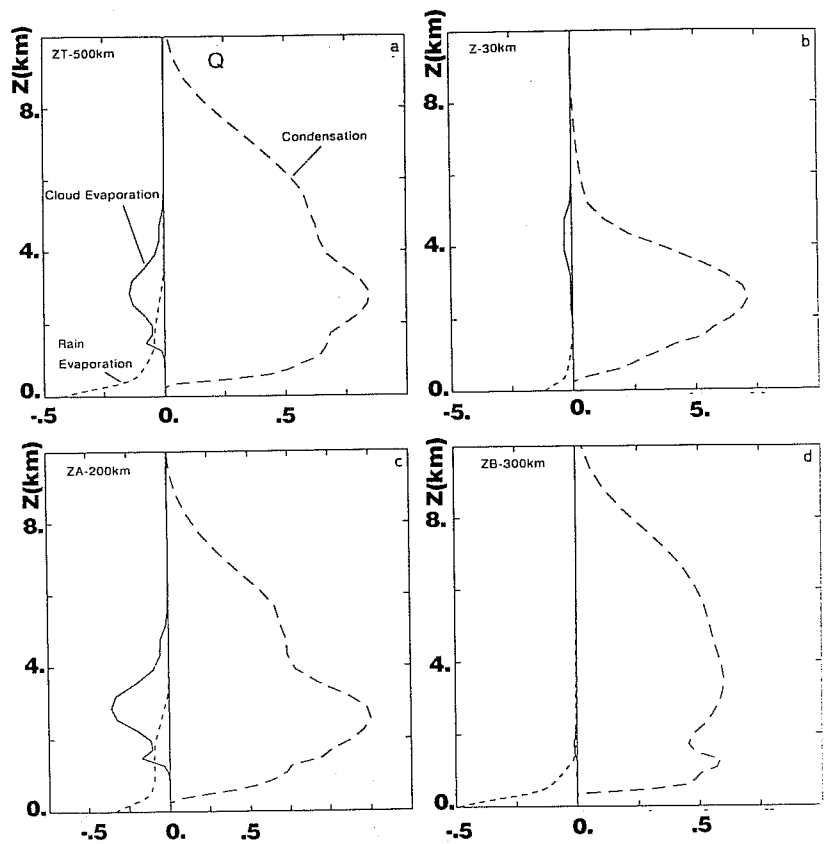

Figure 10: Vertical profiles of latent heating budget for control experiment (IOP2 case), and for the ZT, Z, ZA and ZB zones (see text and Fig. 4) (from Redelsperger and Lafore 1994)

The different contributions to the latent heating Q for the main part ZT of the frontal system are shown in Fig. 10a. The net latent heating indicates a warming due to condensation throughout the troposphere, except below level 600 m, where rain evaporation leads to a cooling maximum of 0.45 °K h^{-1} close to the ground. The analysis of the profiles in the different sub-regions Z, ZA and ZB (Figs. 10b, c, and d) allows the following conclusions:

- The NCFR represents the main contribution (Fig. 10b) to the region ZA(Fig. 10c), up to 4 km.
- In region ZB (Fig. 10d), the WSWR mainly contribute to heating the middle and upper troposphere. However, the secondary frontal discontinuity located in the warm sector also induces a heating at low levels.
- The intense cooling by rain and cloud evaporation mainly results from the trailing precipitation of wide bands, and occurs up to altitudes of 5 km in the cold frontal zone.

6b Apparent heat and moisture sources

In terms of convective parameterization, it is customary to define the apparent heat source Q_1 and the apparent moisture sink Q_2, which are usually calculated from diagnostic analysis of observations. The equations of the present model can be simply related to these quantities by horizontally averaging the tendenciy equations for the potential temperature θ and mixing ratio of water vapor q over the considered region:

$$Q_1 \equiv \langle\pi\rangle \overline{\frac{D\theta}{Dt}}^{Z} = -\frac{\langle\pi\rangle}{\langle\rho\rangle}\overline{\frac{\partial\langle\rho\rangle w''\theta''}{\partial z}}^{Z} + Q + D_{Q_1} \tag{9}$$

$$Q_2 \equiv -\frac{\langle L\rangle}{C_p}\overline{\frac{Dq_v}{Dt}}^{Z} = \frac{\langle L\rangle}{C_p\langle\rho\rangle}\overline{\frac{\partial\langle\rho\rangle w''q_v''}{\partial z}}^{Z} + Q + D_{Q_2} \tag{10}$$

where Q is the latent heating, D_{Q_1} and D_{Q_2} are the subgrid scale diffusion, overbars denote horizontal averaging over the considered zone Z and double quotes the deviations from this average (hereafter called eddy part).

The vertical transport of heat and moisture by all rainbands can be important for some parts of the frontal system (Figs. 11 and 12). In the planetary boundary layer (PBL), the contribution by the subgrid–scale terms is important for all the system and decreases the cloud diabatic effect. This stresses the importance of having a good representation of the PBL in large scale models, which should be coupled with the convection parameterization scheme. The transports by the NCFR (Figs. 11b and 12b) are intense and clearly seen on the scale of the zone ZA (Figs. 11c and 12c). They contribute to heat and reduce the drying at mid–troposphere around 3.5 km, with opposite effects below 2.5 km. They are responsible for the double–peak structure of Q_2 detected in the zone ZA. In the warm sector (Figs. 11d and 12d), the band linked to the secondary frontal discontinuity shows similar effects to the NCFR but on a shallower layer (2.5 km instead of 4.5 km). The impact of transports by bands on the system scale ZT (Figs. 11a and 12a) is less important although not negligible.

These results compare with those obtained for squall line systems (e.g. Lafore *et al.* 1988), for which the eddy transport was found to be more important for Q_2 than Q_1. As a consequence, the Q_2 profile was not well approximated by the latent heating profile Q. Also the Q_2 double–peak structure was found for squall line systems.

Some other similarities with tropical cases are striking. The NCFR effects look like the effects of the convective part of a squall line (Lafore *et al.* 1988), but occur over a shallower depth (4.5 km). The main difference is the absence of double peak structure in the Q_2 profile at this scale.

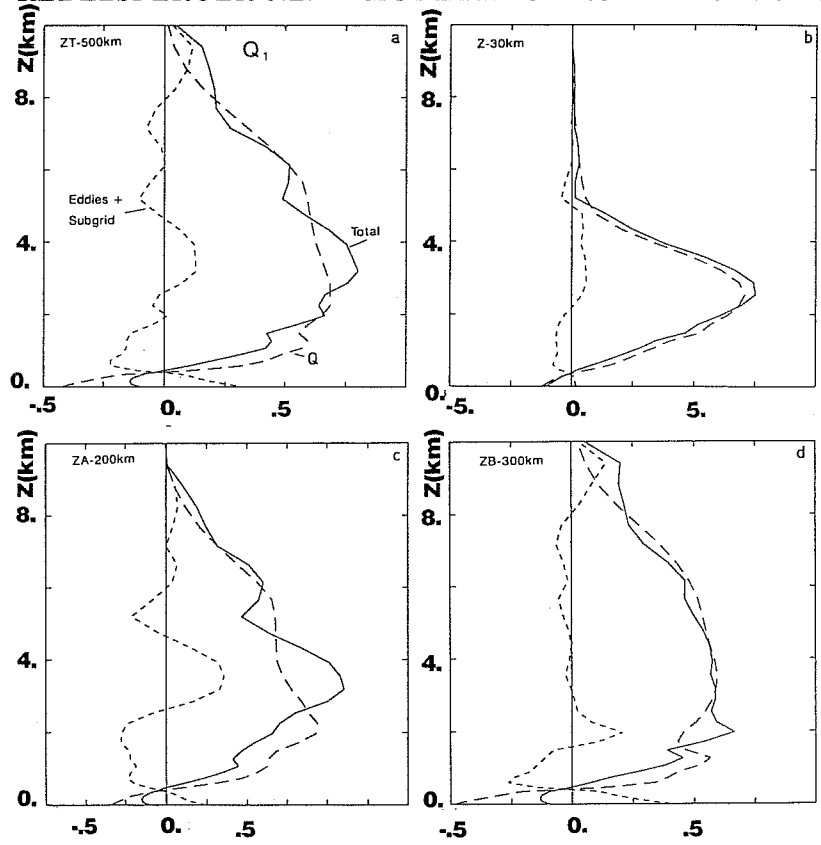

Figure 11: As Fig. 10 but for the apparent heat source Q_1 (in °K h^{-1}). (from Redelsperger and Lafore 1994)

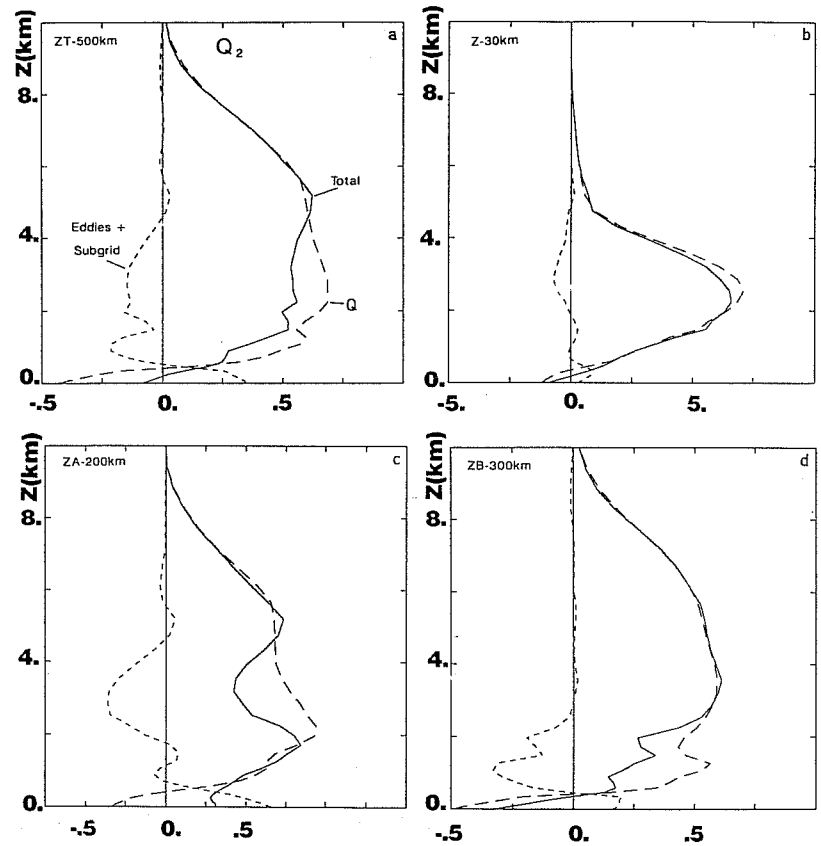

Figure 12: As Fig. 10 but for the apparent moisture sink Q_2 (in °K h^{-1}). (from Redelsperger and Lafore 1994)

The profiles due to the WCFR resemble those of the squall line stratiform part (Caniaux *et al.* 1993a), with cooling/moistening by cloud and rain evaporation occuring at low levels, and heating/drying above. Nevertheless, due to the weakness of precipitation associated with the WCFR, its cooling/moistening layer is much weaker. As suggested by Clough and Franks (1991), the ice phase may be important for enhancing the evaporation beneath the WCFR and for intensifying it. At the system scale (region ZT), the similarities with squall line systems are weaker. Indeed, contrasting with the tropical cases, the net cooling/moistening due to wide bands dominates in the low levels. The Q_2 double peak structure is also weaker for the frontal case, due to the difference of altitude between activity core of narrow and wide bands.

Sensitivity of these results to the model horizontal resolution have been also studied. At the system scale (not shown), no major differences in the Q_1 and Q_2 profiles were obtained for a same experiment but with a 20 km horizontal resolution, in contrast with smaller scales, as the NCFR is not correctly simulated. As seen previously, the 20 km resolution simulation also produced almost the same rainfall rate as the 5 km one (control experiment).

6c Apparent horizontal momentum sources

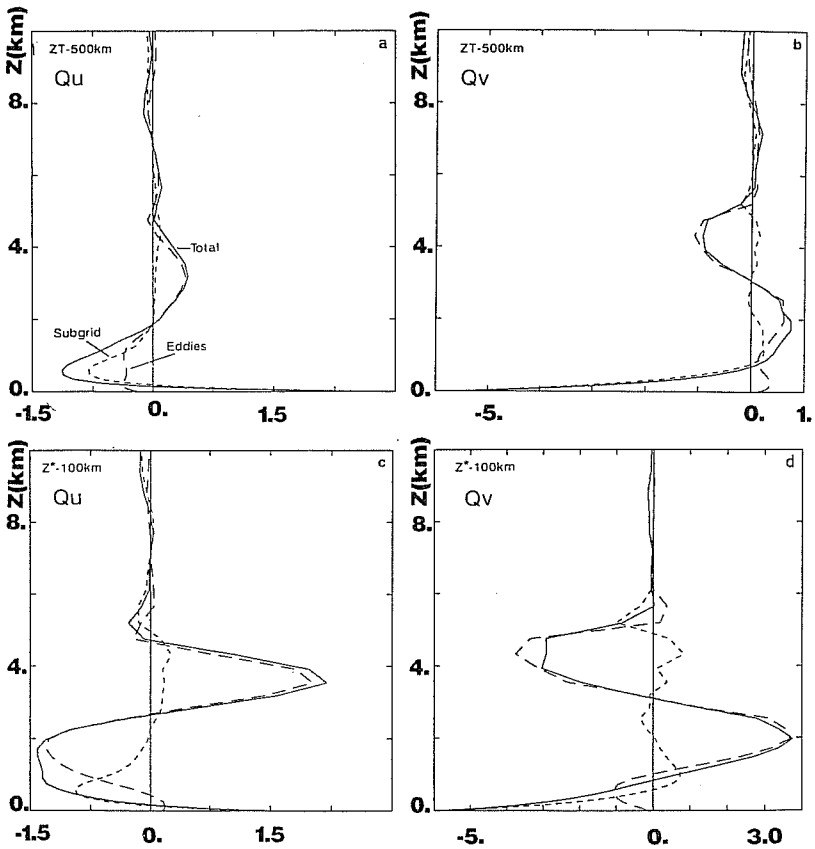

Figure 13: Vertical profiles of apparent cross–front (a, b), and along–front (c,d) momentum sources (Q_u and Q_v respectively) for control experiment (IOP2 case), for the ZT (a, c) and Z* (b, d) zones. Units are in m s^{-1} h^{-1}. (from Redelsperger and Lafore 1994)

Momentum transports by convection remain a difficult and poorly understood part of cloud effects on atmospheric motions at all scales. In this section, the effective contribution by frontal rainbands is computed from the present simulations and discussed. As for heat and moisture, it is possible to define apparent source of cross– and along–front momentum, as follows:

$$Q_u \equiv \frac{\overline{Du}^Z}{Dt} = -\frac{1}{\langle\rho\rangle}\frac{\overline{\partial\langle\rho\rangle w''u''}^Z}{\partial z} + D_{Q_u} \qquad (11)$$

$$Q_v \equiv \overline{\frac{Dv}{Dt}}^Z = -\frac{1}{\langle\rho\rangle}\overline{\frac{\partial\langle\rho\rangle w''v''}{\partial z}}^Z + D_{Q_v} \tag{12}$$

where D_{Q_u} and D_{Q_v} represent the subgrid scale diffusion.

Figures 13a and b show the resulting momentum sources as seen at the system scale (ZT). On average, along–front sources are about 2 to 3 times stronger than the cross–front ones, in particular for the subgrid scale contribution. It is in agreement with recent results (Gueths 1993) obtained from single Doppler radar measurements for four frontal systems, observed during FRONTS87. The subgrid scale contribution is concentrated in the PBL and is rather horizontally homogeneous. It mainly decelerates the along–front flow up to 750 m (maximum of 5.5 m s $^{-1}$ h^{-1}) and slightly accelerates it above.

The most striking feature occurs below 5 km, and is due to intense transports of vertical momentum in the vicinity of the NCFR. This is confirmed by the Q_u and Q_v profiles computed over a box Z* of 100 km width (Fig. 4c), surrounding the NCFR (Figs. 13c and d). Due to a positive correlation between the vertical velocity w and the cross–front velocity u fields (see the NCFR outline superposion Fig. 4e), the vertical flux of cross–front momentum by eddies (Fig. 14c) is significant and positive up to 4.5 km, with a maximum of 0.55 kg m^{-1} s^{-2} at 2.9 km. The resulting Q_u apparent source by resolved eddies (Figs. 13a and c), is thus characterized by deceleration and acceleration below and above 2.9 km, with significant intensity (-0.36 and 0.42 m s^{-1} h^{-1}, respectively at a scale of 500 km). An intensification of the along–front vorticity (cross–front vertical shear), and a decrease of the along–front component of the moist potential vorticity (MPV) results.

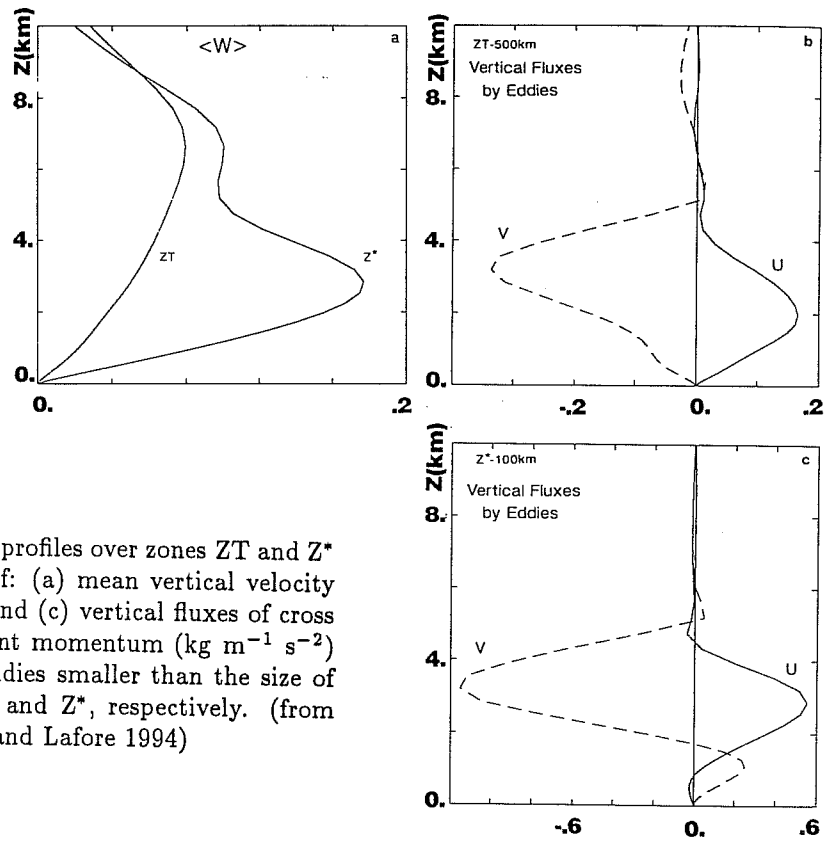

Figure 14: Vertical profiles over zones ZT and Z* (IOP2 case) of: (a) mean vertical velocity (m s^{-1}); (b) and (c) vertical fluxes of cross and along–front momentum (kg m^{-1} s^{-2}) by resolved eddies smaller than the size of the boxes ZT and Z*, respectively. (from Redelsperger and Lafore 1994)

The behaviour of the along–front momentum is similar to the crossfront, but of opposite sign with about a double magnitude. In the NCFR, the w and v fields are negatively correlated (see the NCFR outline superposed on Fig. 4d), and lead to an intense downward flux of along–front momentum (Fig. 14c), with a minimum of -1.2 kg m^{-1} s^{-2} at 3.2 km. The resulting effects (Figs. 13b and d) are thus acceleration and deceleration below and above the level 3.2 km, respectively (0.75 and -1.06

m s^{-1} h^{-1} respectively at a scale of 500 km). As a consequence, the cross-front vorticity as well the cross–front component of the MPV increase. In fact, the vertical redistribution of horizontal momentum by the NCFR occurs in such that the loss of MPV in the along–front direction is partially compensated by the gain of MPV in the cross–front direction. This is in agreement with the MPV conservation, as verified by Bénard *et al.* (1992b) in a budget analysis. This suggests that the antisymmetric structure of the Q_u and Q_v profiles is related to MPV conservation.

In contrast with the Q_1 and Q_2 profiles, the Q_u and Q_v are more sensitive to the horizontal resolution. As shown on Figs. 15, the simulation with a 20 km horizontal resolution reproduces a Q_u profile similar to the control experiment (5 km horizontal resolution) owing to the subgrid scale parameterization, as the NCFR is not explicitly resolved. The former experiment fails to simulate the Q_v profile due to the NCFR, as given by the control experiment.

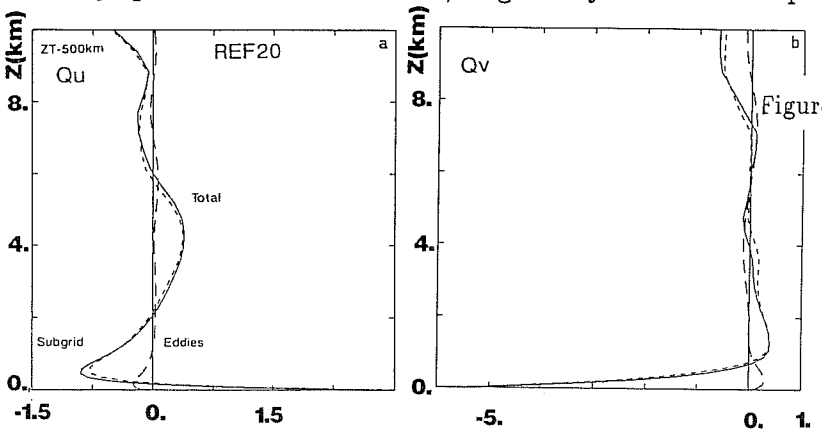

Figure 15: Vertical profiles of apparent cross–front (a), and along–front (b) momentum sources (Q_u and Q_v respectively) for the IOP2 case with a 20 km horizontal resolution and for the ZT zone. Units are in m s^{-1} h^{-1} (from Redelsperger and Lafore 1994)

Concerning the effect of the NCFR on the cross–front momentum field, a dynamical basis for its understanding is provided by the two-dimensional nonlinear and stationary theory of organized convection (Moncrieff 1992). Though this theory does not include the Coriolis parameter, it gives a guideline for understanding this band, which is narrow compared with the Rossby radius of deformation (Moncrieff 1989). The present case is characterized by intense cross–front shear, where the overturning updraught is an important branch of the system, whereas the jump updraught is almost non existent. The simulated positive cross–front momentum flux suggests a downshear-tilted structure for the NCFR, which is in agreement with the simulated overturning updraught.

7 CONCLUSIONS

This study has shown that two–dimensional and three–dimensional nonhydrostatic cloud models can produce detailed and realistic simulations of frontal systems and their sub–structure. Three different cases were simulated: the Eady problem, IOP2 and IOP7 cases of FRONTS87 experiment. In all cases, the model has indeed the ability to reproduce a large variety of observed frontal bands, starting from only the knowledge of mesoα scale fields.

Good Doppler radar observations obtained during the IOP2 of FRONTS87 allowed us to validate the simulations performed in this case. The Narrow Cold–Frontal Rainband (NCFR) was identified as the surface cold front with a maximum of vertical velocity of 1.45 m s^{-1}. Two classes of wide bands were also observed: a wide cold–frontal rainband (WCFR) and warm sector wide rainbands (WSWR) producing precipitation rates weaker than the NCFR, and with weak vertical velocities around .2 m s^{-1}. The results are promising because the simulated structures show strong similarities to the observed one. Particularly, the vertical velocity fields exhibit similar banded features to those of Doppler radar observations. The location, intensity and width of different observed bands were reproduced by the model. The precipitation associated with the NCFR and WSWRs was also close to the observed values. However the present simulation of IOP2 fails to reproduce the precipitation

associated with the WCFR, although this band exists in cloud water content and vertical velocity fields. The underestimation of downdraught underneath this band may be due to the omission of an ice phase parameterization.

An important consequence of the agreement between the control simulation and the observations for the IOP2 case is the possibility of using the simulation to compute heat and moisture budgets. The analysis of the latent heating budget has shown that the NCFR represented the main contribution of heating in the low levels of the frontal region. The wide bands contribute to middle and upper troposphere heating. Important cooling is observed up to 5 km altitude, resulting from cloud evaporation and from the trailing precipitation of wide bands (mainly the WCFR). The budgets of the apparent heat and moisture sources have stressed the importance of the eddy transport, particularly for the apparent moisture source transport. This result was also found in previous studies of squall lines.The eddy transport also induces a double–peak structure in the apparent moisture source.

The analysis of the apparent sources of momentum suggests that the NCFR can significantly affect the large scale flow. This band is tilted downshear and transports positive cross–front momentum upward, leading to an intensification of the along–front vorticity and an overturning updraught. The apparent source of along–front momentum Q_v profile presents an antisymmetric structure to the one of Q_u, but with about the double intensity, which may be qualitatively explained by the property of conservation of MPV. Using dual Doppler radar techniques, Chong *et al.* (1991) have shown that in the NCFR region, a three-dimensional circulation is superposed to the basic cross–front two-dimensional one. Further studies are thus needed on the vertical transport of momentum by the NCFR, through budget analysis of fields issued from Doppler radar analysis and three-dimensional simulations. As suggested by Moncrieff (1989), the theory of momentum transport for squall lines is relevant to narrow cold frontal rainbands, because the relative flow structure is similar in both.

Two shortcomings of these IOP2 simulations are the absence of the ice phase representation and the two–dimensional framework. As recently outlined by Clough and Franks (1991), evaporation of precipitation is important in frontal systems with the ice phase during the FRONTS 87 experiment. For this reason, the ice phase parameterization should be activated in our future frontal simulations, as for the squall line simulations (Caniaux *et al.* 1994a). As shown in Redelsperger and Lafore (1994), the two–dimensional framework is very convenient for studying the relationships between rainbands and along–front large scale gradients. However, to increase the realism of these experiments, three–dimensional simulations with high horizontal resolution in the frontal region are necessary. Preliminary results of three-dimensional simulations of IOP7 case of FRONTS87 were presented, in emphazing on the initialization and coupling problems. From the present results of two-dimensional and three-dimensional experiments, it seems that such three-dimensional experiments have the ability to forecast the occurence of rainbands and other significant mesoscale features (e.g. sharp thermal temperature contrasts, strong surface-level winds and high precipitation rates).

Fine horizontal resolution is necessary to describe the NCFR and its associated sharp peak of precipitation. Nevertheless, crude resolution (say 30 km) appears sufficient to simulate the WSWR, the total precipitation and the profiles of the apparent heat and moisture sources at the system scale. The importance of large scale forcings on convection, which is independent on the horizontal resolution, may explain this rather surprising result. In contrast, the profiles of apparent horizontal momentum sources are less correctly predicted at 20 km resolution (IOP2 case), as they mainly result from intense vertical transports occurring in the NCFR. This was particularly true in our IOP2 simulations for the along–front momentum transport. The cross–front momentum transport was similar, as the subgrid turbulence scheme enabled to well parameterize the eddy term in the simulation with a 20 km resolution, directly resolved in the one with a 5 km resolution.

REFERENCES

Asselin, R., 1972: Frequency filter for time integrations. *Mon. Wea. Rev.*, **100**, 487-490.

Bénard, P. , J.L. Redelsperger, and J. P. Lafore, 1992: Nonhydrostatic simulations of frontogenesis in a moist atmosphere. Part I: General description and narrow frontal rainbands. *J. Atmos. Sci.*, **49**, 2200-2217.

Bénard, P., J.–P. Lafore and J.–L. Redelsperger, 1992: Non–hydrostatic simu lation of frontogenesis in a moist atmosphere. Part II : Moist potential vorticity budget and wide rainbands. *J. Atmos. Sci.*, **49**, 2218-2235.

Browning, K. A., and T. W. Harrold, 1970: Air motion and precipitation growth at a cold front. *Quart. J. Roy. Meteor. Soc.*, **96**, 369-389.

Browning, K.A., 1990: Rain, rainclouds and climate. *Quart. J. Roy. Meteor. Soc.*, **116**, 1025–1051.

Cailly, C., J.–P. Lafore, and J.–L. Redelsperger, 1994: Couplage d'un modèle non-hydrostatique de nuages avec un modèle de prévision à grande échelle. Application au cas de la POI7 de l'expérience FRONTS87. Note du Centre National de Recherches Météorologiques, Groupe de Météorologie à moyenne échelle. A paraitre.

Caniaux, G., J.–L. Redelsperger, and J.–P. Lafore, 1994a: A numerical study of the stratiform region of a fast–moving squall line. Part I: General description, and water and heat budgets. *J. Atmos. Sci.*, **51**, 2046-2074.

Caniaux, G., J.–P. Lafore, and J.–L. Redelsperger, 1994b: A numerical study of the stratiform region of a fast–moving squall line. Part II: Relationship between mass, pressure and momentum fields, and momentum budgets. *J. Atmos. Sci.*, **51**, ??-??.

Carpenter, K. M., 1982: Note on the paper "Radiation conditions for the lateral boundaries of limited area numerical models". *Quart. J. Roy. Meteor. Soc.*, **108**, 717–719.

Chang, C. B., D. J. Perkey and C. W. Kreitzberg, 1981: A numerical case study of the squall line of 6 May 1975. *J. Atmos. Sci.*, **38**, 1601-1615.

Chong, M., G. Jaubert and Nuret M., 1991: Small mesoscale structure of a cold–frontal rainband. *Preprints 25th Int. Conf. on Radar Meteor, AMS*, 181–184.

Clough, S.A. and R. A. A. Franks, 1991: The evaporation of frontal and other stratiform precipitation. *Quart. J. Roy. Meteor. Soc.*, **117**, 1057-1080.

Desroziers G., 1993: Reanalyse ARPEGE/CANARI de l'expérience FRONTS 87. Note du Centre National de Recherches Météorologiques, Groupe de Météorologie à moyenne échelle N 22.

Dudhia, J., 1993: A nonhydrostatic version of the Penn State-NCAR mesoscale model: Validation tests and simulation of an Atlantic cyclone and cold front *Mon. Wea. Rev.*, **121**, 1493-1513.

Frank, W.M., 1983: The cumulus parameterization problem. *Mon. Wea. Rev.*, **111**, 1859-1871.

Gall, R.L., R. T. Williams and T. L. Clark, 1987: On the minimum scale of the surface fronts. *J. Atmos. Sci.*, 44, 2562-2574.

GEWEX Cloud System Study (GCSS) Science Plan, 1994: *International GEWEX Project Office*, 11, 62pp.

Gueths R., 1993: Etude de la dynamique de la couche limite préfrontale au voisinage de fronts froids à partir d'observations d'un seul radar Doppler. 207 pages. Thèse de l'Universite Paul Sabatier - Toulouse - France.

Hobbs, P. V., 1978: Organization and structure of clouds and precipitations on the mesoscale and microscale in cyclonic storms. *Geophys. Space Phys.*, **16**, 741-755.

Houze, R. A., P. V. Hobbs, K. R. Biswas, and W. M. Davis, 1976: Mesoscale rainbands in extra-tropical cyclones. *Mon. Wea. Rev.*, **104**, 868-878.

Hsie, E.-Y., and R. A. Anthes, 1984: Simulation of frontogenesis in a moist atmosphere using alternative parameterizations of condensation and precipitation. *J. Atmos. Sci.*, **41**, 2701-2716.

Johnson, R.H., 1984: Partitioning tropical heat and moisture budgets into cumulus and mesoscale components: Implications for cumulus parameterization. *Mon. Wea. Rev.*, **112**, 1590–1601.

Keyser, D., and R. A. Anthes, 1982: The influence of planetary boundary layer physics on frontal structure in Hoskins-Bretherton horizontal shear model. *J. Atmos. Sci.*, **39**, 1783-1802.

Lafore, J.–P., J.–L. Redelsperger and G. Jaubert, 1988: Comparison between a three–dimensional simulation and doppler radar data of a tropical squall line: transports of mass, momentum, heat, and moisture. *J. Atmos. Sci.*, **45**, 3483–3500.

Lafore, J.–P., J.–L. Redelsperger, C. Cailly and E. Arbogast 1993: Nonhydrostatic simulations of frontogenesis in a moist atmosphere. Part III: Thermal wind imbalance and rainbands. *J. Atmos. Sci.*, **51**, 3467-3485.

Lalaurette, F., 1991: Frontal Cyclogenesis: A study of MFDP/FRONTS87 IOP2 using Peridot. *Preprints 9th Conf. on Numerical wheather prediction, AMS.*

Maddox, R. A., 1980: Mesoscale convective complexes. *Bull. Amer. Meteor. Soc.*, **61**, 1374-1387.

Moncrieff, M.W., 1989: Analytical models of narrow cold–frontal rainbands and related phenomena. *J. Atmos. Sci.*, **46**, 150-162.

Moncrieff, M.W., 1992: Organized convective systems: Archetypal dynamical models, mass and momentum flux theory, and parameterization. *Quart. J. Roy. Meteor. Soc.*, **118**, 819-850.

Parsons, D. B. and P. V. Hobbs, 1983: The mesoscale and microscale structure and organization of clouds and precipitation in midlatitude cyclones. XI: Comparisons between observational and theoretical aspects of rainbands. *J. Atmos. Sci.*, **40**, 2378-2397.

Redelsperger, J.-L., and G. Sommeria, 1981: Méthode de représentation de la turbulence d'échelle inférieure à la maille pour un modèle tri-dimensionnel de convection nuageuse. *Bound.-Layer. Meteor.*, **21**, 509-530.

Redelsperger, J.-L., and G. Sommeria, 1986: Three-dimensional simulation of a convective storm: sensitivity studies on subgrid parameterizations and spatial resolutions. *J. Atmos. Sci.*, **43**, 2619-2635.

Redelsperger, J.-L., and J.-P. Lafore, 1988: A three–dimensional simulation of a tropical squall–line: Convective organization and thermodynamic vertical transport. *J. Atmos. Sci.*, **45**, 1334-1356.

Redelsperger, J.-L., and J.-P. Lafore, 1994: Non-hydrostatic simulations of a cold front observed during the FRONTS87 experiment. *Quart. J. Roy. Meteor. Soc.*, **120**, 519-555.

Ross, B. B., and I. Orlanski, 1978: The circulation associated with a cold front: Part II: Moist case. *J. Atmos. Sci.*, **35**, 445-465.

Sommeria, G., and J. W. Deardorff, 1977: Subgrid scale condensation in models for non precipitating clouds. *J. Atmos. Sci.*, **34**, 344–355.

Tao, W.K. and J. Simpson, 1989: Modeling study of a tropical squall type convective line. *J. Atmos. Sci.*, **46**, 177–202.-

Tao, W.K., J. Simpson, C.-H. Sui, B. Ferrier, S. Lang, J. Scala, M.-D. Chou, and K. Pickering 1993: Heating, Moisture, and water budgets of tropical and midlatitude squall lines: Comparisons and sensitivity to longwave radiation. *J. Atmos. Sci.*, **50**, 673–690.

Thorpe A. J., and S. A. Clough, 1991: Mesoscale dynamics of cold fronts. Part I: Structures described by dropsoundings in Fronts 87. *Quart. J. Roy. Meteor. Soc.*, **117**, 903-941.